Seyedheydari, Fahime; Conley, Kevin; Ylä-Oijala, Pasi; Sihvola, Ari; Ala-Nissila, Tapio

Electromagnetic response and optical properties of anisotropic $CuSbS_2$ nanoparticles

Published in:
Journal of the Optical Society of America B: Optical Physics

DOI:
10.1364/JOSAB.456468

Published: 01/07/2022

Document Version
Peer-reviewed accepted author manuscript, also known as Final accepted manuscript or Post-print

Please cite the original version:
Seyedheydari, F., Conley, K., Ylä-Oijala, P., Sihvola, A., & Ala-Nissila, T. (2022). Electromagnetic response and optical properties of anisotropic $CuSbS_2$ nanoparticles. *Journal of the Optical Society of America B: Optical Physics*, *39*(7), 1743-1751. https://doi.org/10.1364/JOSAB.456468

Electromagnetic Response and Optical Properties of Anisotropic $CuSbS_2$ Nanoparticles

FAHIME SEYEDHEYDARI[1], KEVIN CONLEY[2], PASI YLÄ-OIJALA[3], ARI SIHVOLA[3], AND TAPIO ALA-NISSILA[1,4,*]

[1] Department of Applied Physics, Aalto University, Finland
[2] Department of Chemistry and Materials Science, Aalto University, Finland
[3] Department of Electronics and Nanoengineering, Aalto University, Finland
[4] Interdisciplinary Centre for Mathematical Modelling, Department of Mathematical Sciences, Loughborough University, United Kingdom
[*] Corresponding author: tapio.ala-nissila@aalto.fi

Compiled August 17, 2022

We investigate the electromagnetic response of anisotropic (non-spherical) copper antimony disulfide ($CuSbS_2$) nanoparticles and layers embedded with them using computational methods. To this end we calculate the scattering and absorption efficiencies of oblate spheroidal $CuSbS_2$ nanoparticles using the surface integral equation method. We find strong dependence of the response depending on the anisotropy of the spheroids and their orientation with respect to the electric field polarization of the incoming radiation. Thin spheroids display a sharp plasmonic resonance in the ultraviolet which is only observed for the electric field polarization along the short axis. Fano resonances that appear in the near infrared (NIR) blueshift when the short axis length is reduced and they can be either strongly suppressed or enhanced depending on the relative orientation of the spheroid. We further investigate the optical response of thin layers containing $CuSbS_2$ spheroids at low volume fraction using a Monte Carlo method. We find that response of these layers can be considerably modified by changing the short axis length and the orientation of the particles within the layer with respect to the polarization. Our results demonstrate the potential of anisotropic dielectric particles for polarization-dependent-response applications such as solar devices and NIR sensors.

http://dx.doi.org/10.1364/ao.XX.XXXXXX

1. INTRODUCTION

Copper antimony disulfide ($CuSbS_2$) is a non-toxic, earth-abundant material that occurs naturally as the mineral chalcostibite [1, 2]. It is emerging as a promising photovoltaic material due to its optical band gap that falls within the optimum range for solar cells [3, 4], varying between $1.4 - 1.52$ eV ($0.82 - 0.89$ μm) [5–8]. The fundamental band gaps have been predicted to be indirect in nature; however, the difference between the lowest energy direct and indirect gaps is only of the order of 0.1 eV [9–12]. $CuSbS_2$ has a layered crystal structure and the details of the electronic structure of bulk, monolayer and bilayer $CuSbS_2$ were recently examined using quantum-mechanical Density Functional Theory and many-body perturbation theory [13]. Their results show that regardless of dimensionality the material has a strong absorption coefficient above 1.7 to 1.9 eV and weak optical excitations below the band gap. These effects are attributed to the quantum confinement, electron–hole interactions, and the formation of surface states.

In recent years, $CuSbS_2$ thin films have been prepared and synthesized using various deposition techniques such as sulfurization of an electrodeposited metal stack [14], sputtering [15], solvothermal [5], thermal evaporation [16, 17], chemical bath deposition [18] and hot injection method [5, 7, 8, 19–21]. Most recently, high-quality platelet-like $CuSbS_2$ nanocrystals with a well-defined shape and narrow size distribution were experimentally prepared using an improved hot injection method [8]. The particles are single orthorhombic crystals with space group *Pnma* and a large exposed (001) surface [22]. It is expected that these platelets will directionally scatter light depending on their size and orientation to incident light. Such directional scattering will aid in directing the propagation of light in near-IR applications. This opens up interesting possibilities to engineer nanoparticle shapes and sizes for a specific application.

Interest in layered semiconductor materials has increased in recent years due to quantum-mechanical confinement effects and unique anisotropic scattering. Directional scattering has been successfully used in applications as diverse as optical and biological sensors [23, 24], photocatalysis for solar energy storage [25], solar glazing [26], and thermal energy management [27]. High aspect ratio morphologies, such as two dimensional platelets, are known to exhibit sharp and directional scattering resonances [28]. The shape and composition of the material must be known to precisely predict the propagation of electromagnetic waves in heterophase media.

In recent works we have studied the electromagnetic response of homogeneous, semiconductor@metallic [29], and metallic@semiconductor [30] (core@shell) spherical particles. Our findings have demonstrated that nanoparticles with a low band gap semiconductor core covered by a metallic shell can show pronounced effects of plasmon hybridization. There is a strong interaction between the resonances of the plasmonic metallic shell and the semiconducting core material which allows tuning of the electromagnetic response for near-IR applications. We also calculated the spectral response of layers containing bare and oxide-coated particles under irradiation from solar and blackbody emitters in good agreement with experiments [31, 32]. Most recently we examined the optical response of small $CuSbS_2$ spheres using Lorenz-Mie theory [33]. The absorption and the total scattering efficiencies broaden and shift to longer wavelengths with increasing particle size [33].

While the optical response of a homogeneous sphere in an external electromagnetic field has a closed-form analytic solution as formulated by Lorenz and Mie [28, 34–36], particles with complex geometries must usually be treated with numerical methods, such as the finite difference time domain (FDTD), discrete (coupled) dipole approximation (DDA or CDA), and finite element methods (FEM) [37–39]. Here we adopt the surface integral equation (SIE) method [40–42] to extend our previous work on $CuSbS_2$ spheres to anisotropic (non-spherical) particle shapes. A natural extension from the spherical shape are the superquadrics. From this class of shapes we have chosen to focus on nanoscale oblate spheroids, which have two identical long (major) axes and one short (minor) axis. The SIE method allows accurate calculations of the scattering and absorption efficiencies and scattering albedo of individual particles with different morphologies.

In the present work we first examine in detail the electromagnetic response of spheroids with different orientations with respect to the Poynting vector and polarization of the incoming wave. The properties of spheroidal $CuSbS_2$ nanoparticles surrounded by a non-absorbing insulating medium with a constant refractive index of 1.0 are discussed in Section 3.A. The optical properties of layers embedded with spheroidal $CuSbS_2$ particles of different sizes, orientations, and volume fractions are described in Section 3.B. Our main result is that the scattering and absorption efficiencies that are mainly determined by UV plasmonic and NIR Fano-type resonances are strongly influenced by both particle shape and their orientation with respect to the incoming radiation. This makes it possible to tune details of the wavelength-dependent efficiencies by varying the geometrical parameters and response based on the polarization of the radiation.

2. METHODS

A. Dielectric permittivity of $CuSbS_2$

The frequency-dependent permittivity, $\varepsilon(\omega) = \varepsilon_1(\omega) + i\varepsilon_2(\omega)$, of bulk and monolayer $CuSbS_2$ was taken from a previous study using Density Functional Theory [13] with the Heyd-Scuseria-Ernzerhof (HSE06) hybrid functional [43]. The microscopic dielectric tensor was obtained using the Independent Particle Approximation via a sum over empty Kohn-Sham states (ε_2) and a Kramers-Kronig relation (ε_1) [13]. Here the real and imaginary parts of the bulk and monolayer permittivities were averaged over three orthogonal directions. The monolayer permittivity was used for particles with a thickness or radius less than 5 nm; otherwise the permittivity of the bulk material was used. The averaged dielectric functions are shown in Figures 1 (a) and (b). A schematic of the atomic structure for the bulk of orthorhombic $CuSbS_2$ is shown in Figure 1 (c). The layered structure can be separated into single (2D) and thin multilayer systems.

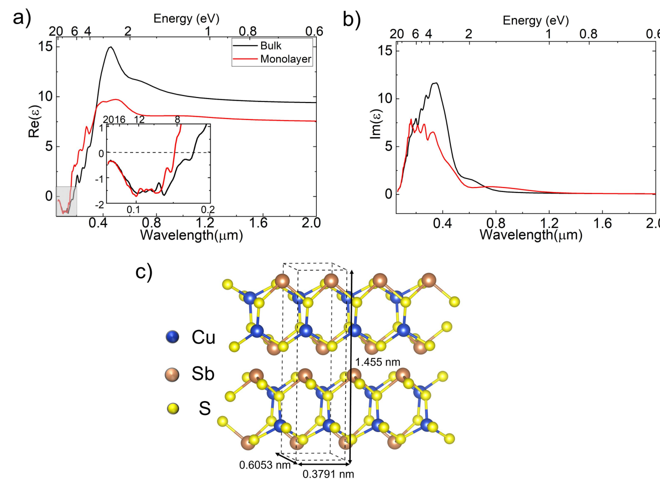

Fig. 1. (a) The real and (b) imaginary parts of bulk (black lines) and monolayer (red lines) $CuSbS_2$ permittivity as a function of wavelength (bottom) and energy (top). The inset shows how $\varepsilon_1 = \mathrm{Re}(\varepsilon)$ becomes negative in the UV region, indicating the possibility of plasmonic resonance type of response. (c) Schematic of the atomic structure of bulk $CuSbS_2$ with Cu, Sb, and S atoms shown as blue, brown, and yellow spheres. The unit cell dimensions are shown.

B. Particle size and morphology

We consider nanoscale $CuSbS_2$ spheroidal particles that belong to the class of superquadrics [44]. The general equation for ellipsoidal particles is given by

$$f(x,y,z) = \left(\frac{x}{R_x}\right)^2 + \left(\frac{y}{R_y}\right)^2 + \left(\frac{z}{R_z}\right)^2, \quad \textbf{(1)}$$

where R_x, R_y, and R_z are semi-axes along the Cartesian coordinate axes x, y, and z. We focus on oblate spheroids that have two identical long axes and one short axis. Unless specified otherwise, the incident electric field is x-polarized and propagates in the z direction. The spheroid is oriented with its short axis along either the x, y, or z direction. This gives rise to two possibilities that we call edge-on and face-on with respect to the propagation direction z. For the edge-on case there are two subclasses, since the short radius can be either along the x axis (edge-on-x) or the y axis (edge-on-y) as shown in Figures 2 (a) and (c), respectively. The face-on case has the short axis along the z direction (Figure 2 (e)).

In addition to the fixed particle orientations described above, we further consider the case where the electric field has an arbitrary angle of incidence ϕ with respect to a spheroid. This angle refers to the angle between the propagation direction and the z axis of the coordinate system, and varies between 0 and 90 degrees as shown with red arrows in Figure 2 (g). The electric field of an incident wave can be either in the xz plane (shown with blue arrows in Figure 2 (g)) or parallel to the y direction.

The electromagnetic response from individual spheroids can further be used to model the properties of compact layers containing embedded particles using a Monte Carlo method by tracing the path of single-photon packages inside the layer that launched perpendicularly into the layer. The schematics of the four cases considered in this work are in Figures 2 (b), (d), (f), and (h). The incoming radiation is shown by the black arrow in Figure 2 (b) and is perpendicular to the layer. The layers have thickness T equal to 200 μm.

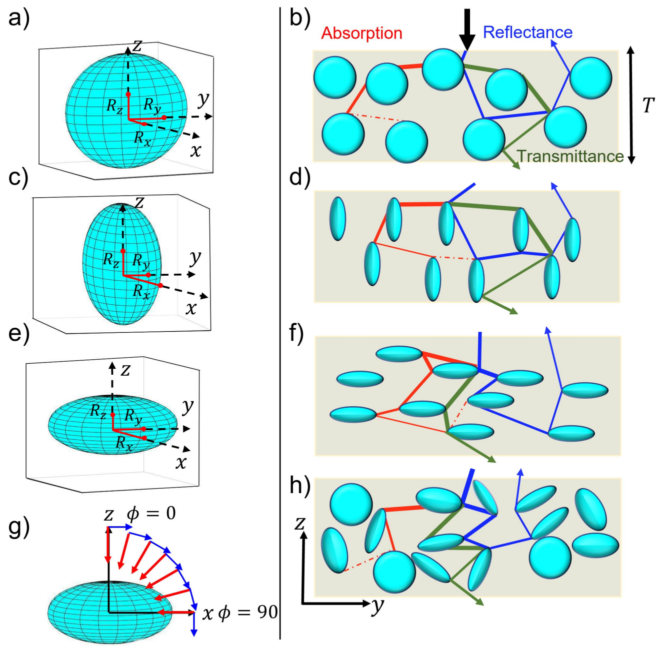

Fig. 2. Spheroid morphologies with their short axis along the (a) x, (c) y, and (e) z direction. Panels (a) and (c) are denoted edge-on-x and edge-on-y, respectively, and (e) is face-on. (g) Red arrows denote the direction of an incoming wave for an arbitrary angle of incidence ϕ with respect to the z axis. The blue arrows indicate the polarization of the incident electric field, which in this schematic is in the xz-plane. Panels (b), (d), (f) and (h) are schematics of the radiative transport in a layer of thickness T. The particles are oriented with their short axis in (b) x, (d) y, (f) z, and (h) random directions. The black arrow indicates the path of an incoming photon which consequently is absorbed (red trajectory), reflected (blue trajectory), or transmitted through the layer (green trajectory).

C. Numerical solutions for scattering and absorption cross sections

The optical response of a spheroidal nanoparticle in an incident electromagnetic field is calculated using the SIE method. For a given incident field, $\vec{E}_{\text{inc}}, \vec{H}_{\text{inc}}$, the method finds equivalent electric and magnetic surface current densities on the surface of the particle. The field scattered by the particle, $\vec{E}_{\text{sca}}, \vec{H}_{\text{sca}}$, can then be computed using these currents. Once the scattered field is available, we may compute the scattering and absorption cross sections, given by

$$\sigma_{\text{sca}} = \frac{P_{\text{sca}}}{S_{\text{inc}}}, \tag{2}$$

and

$$\sigma_{\text{abs}} = \frac{P_{\text{abs}}}{S_{\text{inc}}}, \tag{3}$$

where P_{sca} and P_{abs} are the scattering and absorption powers, respectively, and S_{inc} is the power density of incident wave. The scattering (P_{sca}) and extinction (P_{ext}) power [28, 45] can be computed from

$$P_{\text{sca}} = \frac{1}{2}\text{Re}\int_A (\vec{E}_{\text{sca}} \times \vec{H}^*_{\text{sca}}) \cdot \hat{n}\, dA; \tag{4}$$

$$P_{\text{ext}} = -\frac{1}{2}\text{Re}\left(\int_A (\vec{E}_{\text{sca}} \times \vec{H}^*_{\text{inc}}) \cdot \hat{n}\, dA + \int_A (\vec{E}_{\text{inc}} \times \vec{H}^*_{\text{sca}}) \cdot \hat{n}\, dA\right), \tag{5}$$

where A is a spherical surface in the far field, $\vec{H}^*$ denotes the complex conjugate of $\vec{H}$, and $\hat{n}$ is the exterior unit normal vector of A. The absorbed power is then obtained as

$$P_{\text{abs}} = P_{\text{ext}} - P_{\text{sca}}. \tag{6}$$

For a plane wave, $\vec{E}_{\text{inc}}(\vec{r}) = \vec{E}_0 \exp(ik\hat{k} \cdot \vec{r})$, with E-field polarization $\vec{E}_0$, propagation direction $\hat{k}$ ($|\hat{k}| = 1$) and wave number $k = \omega\sqrt{\varepsilon\mu}$, the power density S_{inc} is given by

$$S_{\text{inc}} = \frac{|\vec{E}_0|^2}{2\eta}, \tag{7}$$

where $\eta = \sqrt{\mu/\varepsilon}$ is the wave impedance of vacuum. The scattering and absorption efficiencies are

$$Q_{\text{sca,abs}} = \frac{\sigma_{\text{sca,abs}}}{G}, \tag{8}$$

where G is the particle cross-sectional area projected onto a plane perpendicular to the incident beam. The scattering or absorption cross sections per unit area, $\sigma_{\text{sca,abs}}$, characterize how efficiently a particle scatters or absorbs radiation.

D. Multipole expansion coefficients for spheroids

As mentioned in the Introduction, scattering by a sphere can be easily solved by Lorenz-Mie theory. In this theory, the incident, scattered, and transmitted fields are expanded with the vector spherical harmonic functions, known also as the multiple expansion. The coefficients of these expansions are determined by enforcing the electromagnetic interface conditions on the surface of the sphere. Next we show how this expansion can be utilized in the scattering analysis of non-spherical particles.

Let us expand the incident electric field using the following truncated multipole expansion

$$\vec{E}_N^{\text{inc}} = \sum_{n=1}^{N}\sum_{m=-n}^{n}\left(a_{nm}^{\text{in}}\vec{M}_{nm}^{\text{in}} + b_{nm}^{\text{inc}}\vec{N}_{nm}^{\text{in}}\right), \tag{9}$$

where $\vec{M}_{nm}^{\text{in}}$ and $\vec{N}_{nm}^{\text{in}}$ are the incoming vector spherical harmonic functions. Similarly, the scattered electric has the following expansion

$$\vec{E}_N^{\text{sca}} = \sum_{n=1}^{N}\sum_{m=-n}^{n}\left(\underbrace{\tilde{a}_{nm}^{\text{sca}}a_{nm}^{\text{in}}}_{a_{nm}^{\text{sca}}}\vec{M}_{nm}^{\text{out}} + \underbrace{\tilde{b}_{nm}^{\text{sca}}b_{nm}^{\text{in}}}_{b_{nm}^{\text{sca}}}\vec{N}_{nm}^{\text{out}}\right), \tag{10}$$

with the outgoing vector spherical harmonic functions $\vec{M}_{nm}^{\text{sca}}$ and $\vec{N}_{nm}^{\text{sca}}$. In the case of a sphere, $\tilde{a}_{nm}^{\text{sca}}$ and $\tilde{b}_{nm}^{\text{sca}}$ are the usual "Mie coefficients" [28].

Then let $\vec{E}^{\text{sca}}$ denote the field scattered by a non-spherical particle computed with the SIE method. Our aim is to expand this scattered field using the multipole expansion. By requiring that $\vec{E}^{\text{sca}} = \vec{E}_N^{\text{sca}}$ on the surface of a sphere far enough from the particle, and by utilizing the orthogonality properties of the vector spherical harmonics [28], the multiple coefficients of the scattered field can be found as

$$a_{mn}^{\text{sca}} = \frac{\int_A (\vec{M}_{mn}^{\text{out}})^* \cdot \vec{E}^{\text{sca}}\, dA}{\int_A (\vec{M}_{mn}^{\text{out}})^* \cdot \vec{M}_{mn}^{\text{out}}\, dA} \quad \text{and} \quad b_{mn}^{\text{sca}} = \frac{\int_A (\vec{N}_{mn}^{\text{out}})^* \cdot \vec{E}^{\text{sca}}\, dA}{\int_A (\vec{N}_{mn}^{\text{out}})^* \cdot \vec{N}_{mn}^{\text{out}}\, dA}, \tag{11}$$

for all $n = 1, \ldots, N$ and $m = -n, \ldots, n$. With these coefficients we may investigate how each multipole term contributes to the scattered field.

E. Optical properties of layers containing particles

Monte Carlo simulations provide an efficient method of determining the optical properties of thin layers containing large numbers of particles. The transmittance, reflectance, and absorption of the layer were simulated using a modified Monte Carlo method [46] originally developed by Wang *et al.* [47]. The path and termination result of 10^7 photons from an infinitesimally small beam normal to the surface of the layer are recorded. The particles are embedded in a non-absorbing medium with a refractive index of 1.0 and the layer is surrounded by air. The layer has a thickness T equal to 200 μm and contains nanoparticles at volume fraction f (equal to 0.01% in most cases). The grid resolution was dz = 2 μm and dr = 1 μm for the axial and radial directions, respectively.

The scattering and absorption coefficients per unit length of a layer containing spheres, μ_{sca} and μ_{abs}, are given by [46]

$$\mu_{\text{sca,abs}} = \frac{3}{2} \frac{f\, Q_{\text{sca,abs}}}{2R}, \tag{12}$$

where R is the radius of the sphere. Correspondingly, the scattering and absorption coefficients per unit length of a layer containing spheroids are given by

$$\mu_{\text{sca,abs}}^{\text{s}} = \frac{f\, \sigma_{\text{sca,abs}}}{V}, \tag{13}$$

where V is the volume of the spheroid. The particle scattering asymmetry factor for a spheroid is given by

$$g = \frac{1}{(\sigma_{\text{sca}} |\vec{E}_0|^2)} \int_A |\vec{E}_{\text{sca}}|^2 \cos(\theta)\, dA. \tag{14}$$

In the layer containing randomly oriented particles, we use the ensemble averaged particle asymmetry factor [48]

$$\bar{g} = \frac{\sum_i \sigma_{\text{sca,i}}\, g_i}{\sum_i \sigma_{\text{sca,i}}}. \tag{15}$$

The optical constant of a layer containing spheroidal particles is obtained from the Maxwell-Garnett effective medium theory. For a low volume fraction, the effective dielectric permittivity of the layer containing randomly oriented spheroids, ε_{eff}, is given by [49]

$$\varepsilon_{\text{eff}} = \varepsilon_{\text{m}} + \varepsilon_{\text{m}} \frac{f}{3} \sum_{j=x,y,z} \frac{\varepsilon_{\text{p}} - \varepsilon_{\text{m}}}{\varepsilon_{\text{m}} + N_j(\varepsilon_{\text{p}} - \varepsilon_{\text{m}})}, \tag{16}$$

where ε_{p} and ε_{m} are the dielectric permittivities of the particle and medium, respectively, and N_j are the depolarization factors of the spheroid. The depolarization factors are discussed in Section 1 of the Supplemental document.

The effective permittivity for uniformly oriented spheroids in the layer is determined by the depolarization factor in the direction of the electric field E_x,

$$\varepsilon_{\text{eff,x}} = \varepsilon_{\text{m}} + \varepsilon_{\text{m}} f \frac{\varepsilon_{\text{p}} - \varepsilon_{\text{m}}}{\varepsilon_{\text{m}} + (1-f) N_x(\varepsilon_{\text{p}} - \varepsilon_{\text{m}})}. \tag{17}$$

We note that when we consider a layer containing randomly oriented spheroids, the cross-sections are averaged over all incident angles.

3. RESULTS AND DISCUSSION

A. Oblate nanospheroids

In this work, calculations of the absorption and scattering efficiencies of individual spheroid were performed by using a computer code employing the SIE method. In the following we consider oblate spheroidal $CuSbS_2$ nanoparticles whose long axes are fixed to 100 nm in length and the short axis varies from $4-75$ nm, in the wavelength range $\lambda = 0.1$ to 1 μm which covers UV and visible frequency bands. For comparison, the scattering and absorption efficiencies of a sphere with a radius of 100 nm are shown in Figure 3. The particles are illuminated by a plane wave with its Poynting vector in the $+z$ direction and the electric polarization is along the $+x$ direction, i.e., $\hat{k} = \hat{e}_z$ and $\vec{E}_0 = \hat{e}_x$ with $|\vec{E}_0| = 1$ V/m. Thus, the orientation of the spheroid with respect to this reference Cartesian system is such that the short axis is either in the x, y or z direction, corresponding to the edge-on-x, edge-on-y, and face-on cases, respectively, as explained in Section 2.B (cf. Figure 2). Our primary interest is to explain the effect of particle orientation on its optical response.

The absorption and scattering efficiencies of the nanoparticles are shown in Figure 3 for the three different orientations. The scattering efficiency of the 100 nm reference sphere depicts two peaks in the NIR regime at $\lambda = 0.596$ and 0.708 μm that are Fano resonances associated with the electric and magnetic dipole modes, respectively [33]. This will be discussed in more detail below. On the other hand, the first general feature evident in the absorption efficiency data is that the maxima shift to shorter wavelengths with decreasing the particle size for the short axis in the x, y, or z directions as shown in Figures 3 (a), (c), and (e), respectively.

Interestingly, the scattering and absorption efficiencies of the edge-on-x case are distinctly different from the other two for small wavelengths. This difference can be explained by the direction of the electric field which is x-polarized. The spheroids with edge-on-x are aligned such that the short axis is parallel to the polarization of the electric field. In this orientation the electric field sees an effectively thinner spheroid that those in the edge-on-y and face-on orientations and the difference is thus more pronounced for thinner particles. The spectral changes of the scattering and absorption efficiency due to flattening of the face are described in Section 1 of the Supplemental document.

In the edge-on-x orientation in Figures 3 (a) and (b), the absorption and scattering efficiencies exhibit a sharp peak at the shortest wavelengths $\lambda < 0.2$ μm. These sharp peaks are associated with localized surface plasmon resonances (LSPRs) of $CuSbS_2$ as indicated by the negative values of $\text{Re}(\varepsilon)$ in Figure 1.

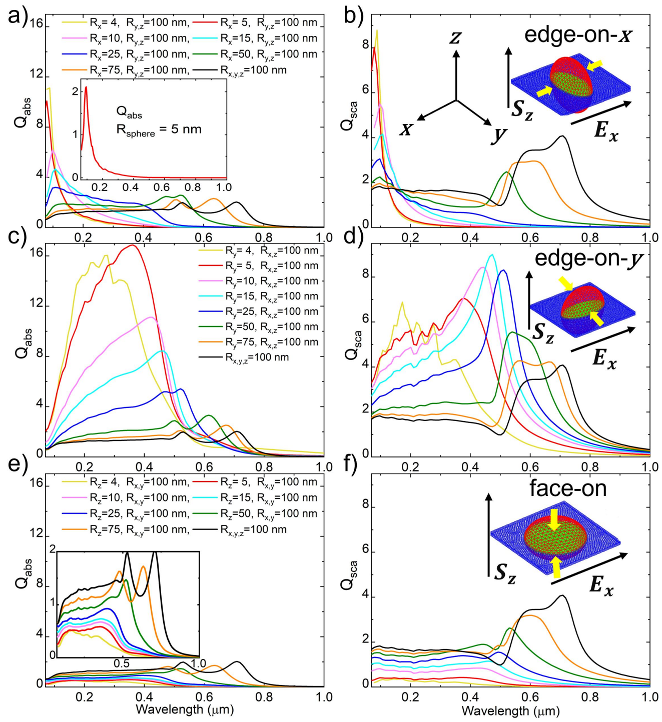

Fig. 3. Absorption and scattering efficiencies of spheroidal particles oriented (a, b) edge-on-x, (c, d) edge-on-y, and (e, f) face-on. The long axes are equal to 100 nm and the short axis varies as 4, 5, 10, 15, 25, 50, or 75 nm. S_z and E_x are the Poynting vector and polarization of the incoming radiation, respectively, in z and x directions. Yellow arrows indicate the short axis direction of particles. The inset in panel (a) shows a sharp peak at short wavelengths in the absorption efficiency of a sphere of radius 5 nm. The inset in panel (e) displays a zoomed-in view of the vertical axis.

As shown in the inset of Figure 3 (a), for the five nanometer thin spheroid the LSPR type of peak at $\lambda = 0.09$ μm is very similar to that of a five nanometer sphere at $\lambda = 0.08$ μm.

To provide more details on the plasmonic properties of $CuSbS_2$, we plot the dielectric function, $\varepsilon(\omega)$, and energy-loss function, $L(\omega)$, in terms of energy in Figure 4. The energy-loss function $L(\omega)$ is given by [50, 51]

$$L(\omega) = \frac{\varepsilon_2(\omega)}{[\varepsilon_1(\omega)^2 + \varepsilon_2(\omega)^2]}. \quad \textbf{(18)}$$

The energy-loss function is proportional to the energy lost by an electron travelling through the material. A peak in the energy loss function spectrum is identified as a possible plasmon peak [12]. $CuSbS_2$ indeed has a major peak in the loss spectrum at 19.40 eV ($\lambda = 0.063$ μm) where the real part of the permittivity is negative and imaginary part is small indicating small losses (Figure 4).

From the point of view of NIR applications the behavior of the Fano resonances here is particularly interesting. For both the edge-on-x and face-on orientations the Fano resonances move to shorter wavelengths as function of decreasing short axis length, and they are highly suppressed for the thinnest spheroids here. In contrast, for the edge-on-y case in Figure 3 (d) the Fano resonances become significantly enhanced until they eventually broaden for the thinnest spheroids. This striking difference demonstrates the sensitivity of the Fano peaks to the geometry and relative orientation of the particles.

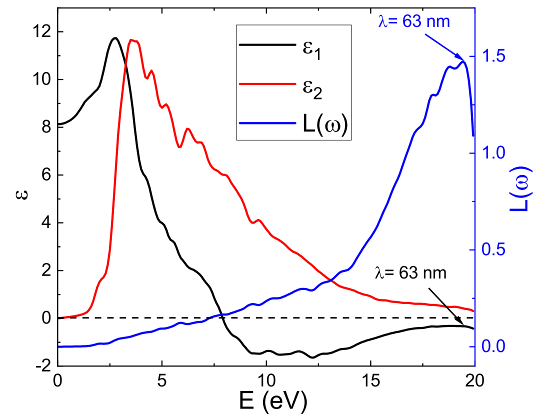

Fig. 4. The real (black line), imaginary (red line) parts, and the electron energy loss function (blue line) of the bulk permittivity as a function of the energy of $CuSbS_2$.

The magnitude of the total electric field distribution $|\vec{E}(x,y)|$ at $\lambda = 0.096$ μm is presented in Figure 5 where the magnitude of the incident field is $|\vec{E}_0| = 1$ V/m. The total field comprises incident, scattered, and internal field components of the full solution to the Maxwell's equations. It can be seen that the total field near the particles becomes highly localized outside the particle in the vicinity of the edges where the curvature is high, while it is negligible inside the particles. This behavior is characteristic of an enhanced LSPR peak.

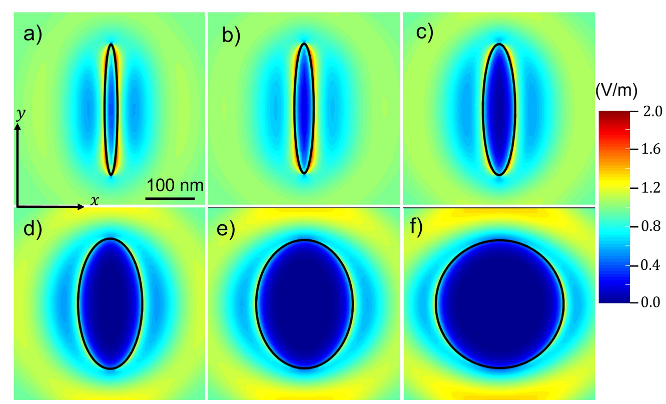

Fig. 5. Magnitude of the total electric field $|\vec{E}(x,y)|$ in and around the spheroidal nanoparticles for the edge-on-x case in Figure 3. The long axes are 100 nm and the short axis varies as (a) 10 , (b) 15 , (c) 25 , (d) 50 , and (e) 75 nm along the x direction. (f) The case of a 100 nm sphere. The wavelength of incident light is 0.096 μm.

To further analyze the nature of the resonances, we computed the multipole expansion coefficients of the scattered electric field as described in Section 2.D. Figure 6 shows these coefficients up to order $N = 4$ in the edge-on-x case. In the figure, the horizontal axis is the wavelength of an incident plane wave and the vertical axis is the short x axis of the spheroid. The short axis is varied from 10 nm (corresponding to the value 0.1 on the vertical axis) to 100 nm (value 1.0), i.e., a sphere. For a sphere, it was earlier shown that there is a clear separation of electric and magnetic dipolar modes that dominate the two long wavelength peaks [33]. However, this situation changes for the case of spheroids. We find that for the edge-on-x case the dipolar modes still dominate the long wavelength Fano peaks ($\lambda > 0.2\ \mu$m) for larger radii, but the contribution from higher modes becomes significant for smaller ones. Correspondingly, for the short wavelength LSPR peak there is strong mixing of the dipolar modes with the higher ones. We note that the contribution from higher modes becomes more pronounced at energies above the band gap (1.71 eV, 0.725 μm).

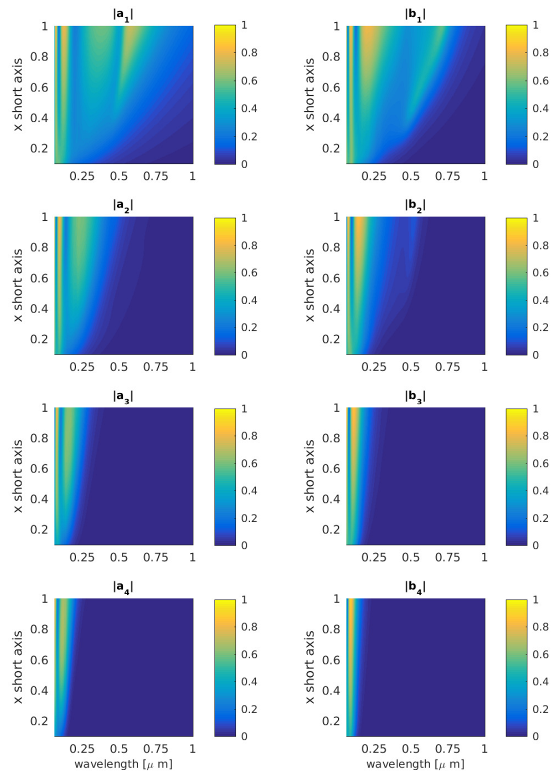

Fig. 6. Multipole expansion coefficients up to order $N = 4$ versus wavelength of an incident plane wave (horizontal axis) and short axis of a spheroid (vertical axis) for the edge-on-x case. The vertical axis is scaled such that value 1.0 corresponds to a sphere with radius 100 nm, and 0.1 is a spheroid with $R_x = 10$ nm, $R_y = R_z = 100$ nm.

In the edge-on-y case in Figures 3 (c) and (d), there is no distinct LSPR at short λ due to the alignment of the electric field with the long axis. The dipolar Fano peaks at long λ for absorption and scattering blueshift with decreasing size as already mentioned, but they broaden with increasing magnitude around 0.5 μm. In addition, the enhanced scattering efficiency for $R_y = 10, 15$, and 25 nm has sharp peaks. Analysis of multipole expansion shows that these Fano peaks are due to overlapping electric and magnetic dipolar modes.

The magnitude of the total electric field at the corresponding Fano scattering maxima for short axis of 10, 15, and 25 nm are shown in Section 2 of the Supplemental document. The total electric fields confirm the existence of the dominating dipole modes at the surface of the spheroids at long wavelengths, $\lambda > 0.4\ \mu$m and very clearly show how the field is focused close to the (semi-)sharp edges of a particle. The distribution of the total internal electric field exists within the interior of the thick particle but is negligible for the thinnest spheroid. This is due to the confinement of the spatial volume.

Finally, in the face-on orientation in Figures 3 (e) and (f), the electric field is again aligned along the long axis and there is no visible LSPR at short λ. Similar to the edge-on-y case, the dipolar Fano peaks at longer wavelengths blueshift with decreasing particle radius. However, their magnitude weakens. The efficiency $Q_{\mathrm{abs,sca}}$ is the ratio of the cross-sectional $\sigma_{\mathrm{abs,sca}}$ and the geometric area with respect to the propagation direction (z) which is $\pi R_x R_y$. The geometric area of the face-on orientation is therefore larger than that of the edge-on orientations. This geometric effect is more pronounced in the scattering and absorption cross-sections for oblate spheroids with arbitrary angles of incidence (Fig. S3) in Section 3 of the Supplemental document.

B. Layers containing oblate spheroids

This section describes the spectral characteristics of thin layers of thickness 200 μm containing $CuSbS_2$ spheroids computed using Monte Carlo modeling (see Section 2.E). The spheroidal particles are dispersed within the layers in four orientations: randomly oriented or uniformly oriented with either edge-on-x, edge-on-y, or face-on (Figures 2 (b), (d), (f), and (h)). The optical constants of these layers are obtained from the Maxwell-Garnett effective medium theory (see Section 2). The layers are examined for different particle size, orientations, and volume fractions f.

B.1. Randomly oriented particles

To gain insight into a layer containing randomly oriented spheroids, we study a simple model obtained by averaging over all possible particle orientations as discussed in Section 2.E. We calculate the scattering and absorption cross-sections of oblate spheroids with an arbitrary angle of incidence for the incoming radiation (see section 2 of the Supplemental document). The average cross-sections are plotted with a dashed black line in Fig. S3 in Section 3 of the Supplemental document.

The absorption and scattering coefficients and the calculated spectra of layers containing spheroids with long axes 100 nm and short axis either 5 nm or 50 nm are shown in Figure 7. The layer containing the smaller $CuSbS_2$ spheroids absorbs strongly in the UV region (80% for $\lambda < 0.4\ \mu$m even at low volume fraction) where absorption becomes the dominant photon transport mechanism (Figure 7 (c)). This trend is also seen in the single particle properties (Figure 3). The transmittance of the layers is more than 95% at wavelengths above the $CuSbS_2$ band gap ($\lambda > 0.8\ \mu$m), where the absorption is almost zero.

Despite the large spheroids having larger absorption and scattering cross-sections, the smaller spheroids are more effective photoabsorbers. This can be attributed to the physical volumes of the spheroids (Eq. (13)). It is particularly noticeable for $\lambda < 0.5\ \mu$m where the absorption is weak for layers containing larger spheroids (Figures 7 (b) and (d)). Therefore, these small spheroids would serve as excellent photoabsorbers in the UV region. However, larger particles are more effective at scattering as shown by the large intensity Fano resonances in the NIR. The reflectance is thus more pronounced in layers containing larger particles.

B.2. Fixed particle orientations

Since significant differences were observed in the optical properties of the individual particles after a change in orientation,

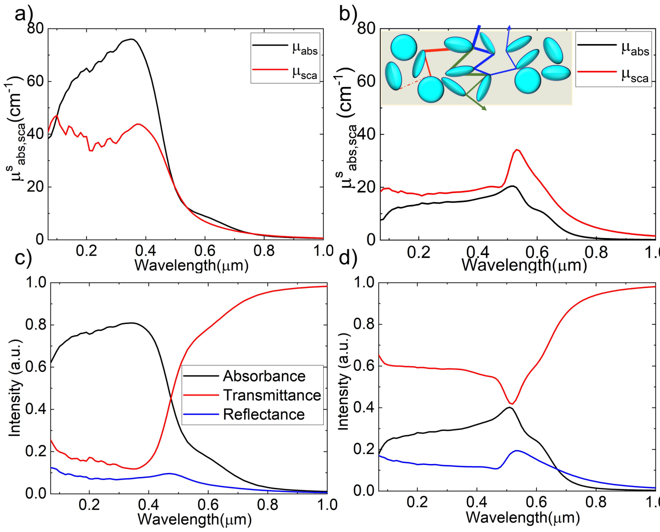

Fig. 7. The absorption and scattering coefficients of randomly oriented spheriodal particles with their long axes 100 nm and short axis (a) 5 nm and (b) 50 nm. The transmittance, absorbance, and reflectance spectra of a 200 μm thick layer embedded with spheroidal particles with long axes 100 nm and short axis (c) 5 nm and (d) 50 nm at a $f = 0.0001$ volume fraction. The inset in panel (b) shows a schematic of a randomly oriented configuration from Figure 2 (h).

we next consider layers containing particles with fixed orientation. The reflectance, transmittance, and absorbance spectra are computed for three layers containing spheroidal $CuSbS_2$ nanoparticles uniformly in the edge-on-x, edge-on-y, or face-on orientations (Figures 8 (a), (b), and (c), respectively). The long axes of the particles are 100 nm and the short axis 5 nm, and at $f = 0.0001$ (0.01%) volume fraction.

The different orientations of the embedded spheroids in the layers significantly change the absorption onsets. In Figure 8 (a), the absorbance of the layer containing spheroids with their short axis in the x direction starts to rapidly increase below $\lambda \approx 0.4$ μm. By stark contrast, the onset of absorption in layers containing spheroids with their short axis in the y or z directions is redshifted to $\lambda \approx 0.8$ μm. The onset is also different for layers containing randomly oriented particles (Figure 7). Thus, when the particles are oriented with their short axis along y, z or randomly, there absorbance is greatly enhanced between $\lambda \approx 0.2 - 0.4$ μm. Additionally, the particles have higher scattering efficiency which results in stronger reflectance. This behavior in layers is expected based on the scattering and absorption efficiencies of the individual nanoparticles (cf. Figure 3). Note that reflection from the layers is largely determined by diffuse reflection and there is very little specular reflection. Similarly, all layers are characterized by a reduced absorption and increasing transmittance above the $CuSbS_2$ band gap wavelength. The results show how the optical properties in the layers can be tuned by changing the relative orientation of the spheroidal particles.

B.3. Volume fraction effect on the plasmonic peak

We have shown above that a single thin spheroid oriented edge-on-x has a strong LSPR type of peak in the UV region. We investigate a layer dispersed with such spheroids at finite volume fraction (cf. Figure 2 (b)). The $CuSbS_2$ spheroidal particles

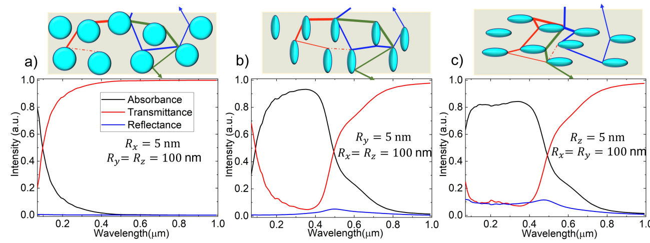

Fig. 8. Calculated optical properties of a 200 μm thick layer embedded with spheriodal particles whose long axes are 100 nm and short axis is 5 nm in the (a) x, (b) y, and (c) z direction at $f = 0.0001$ (0.01%) volume fraction. The schematics above the panels are taken from Figures 2 (b), (d), and (f).

have long axes of 100 nm and short axis of $R_x = 5$ nm, and the volume fraction f varies from 0.0001 to 0.1 (from 0.01% to 10%). The absorbance onset shifts to longer wavelengths with increasing volume fraction as shown in Figure 9. The plasmonic peak observed in the absorption efficiency of the single particle (Figure 3 (a)) is only clearly identifiable in absorbance at the lowest volume fraction, $f = 0.0001$, (Figure 9 (b)). Thus the plasmonic peak is obscured at larger volume fractions. As expected from Eq. (13), increasing the volume fraction considerably increases both absorption coefficients and absorbance (Figures 9 (a) and (b)). The absorption coefficient maximum increases by a factor of 1000 from $f = 0.01\%$ to $f = 10\%$.

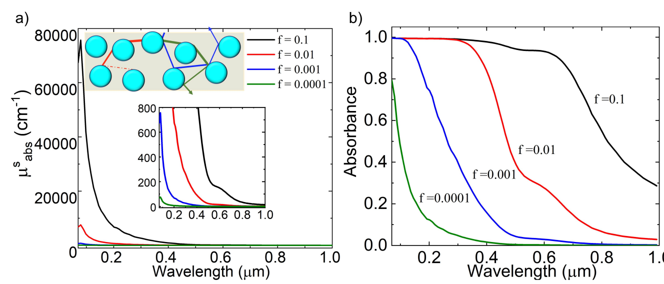

Fig. 9. Effect of the increase in the volume fraction on the absorption coefficient and absorbance. The absorption coefficient (a) and the absorbance (b) of spheriodal particles with long axes 100 nm and short axis $R_x = 5$ nm. The volume fraction varies from 0.1 to 0.0001. The inset in panel (a, top) is taken from Figure 2 (b). The inset in panel (a, bottom) displays a zoomed-in view of the vertical axis.

4. CONCLUSIONS

In this work, we have extended our previous work on the optical and NIR response of spherical $CuSbS_2$ nanoparticles to the case where these particles are strongly geometrically anisotropic, with an oblate spheroidal shape. Due to the shape and orientation these particles exhibit considerable differences in their electromagnetic response, in particular when the short axis is parallel to the polarization vector of the incident electric field. In this case there is a strong LSPR type of peak for nanoscopically thin spheroids at short wavelengths $\lambda < 0.2$ μm. In contrast to spherical particles whose radius equals the short axis of the spheroid, the LSPR peak is accompanied by strong mixing of the dipolar modes with the higher ones. Of particular interest to NIR applications is the strikingly strong dependence of the

Fano resonances on the relative orientation and geometry of the particles. As seen in Figure 3(d), for the edge-on-y orientation the Fano peaks are actually enhanced when blueshifting with decreasing short axis length. We have also examined the response of 200 μm thick layers embedded with spheroids using effective medium theory and Monte Carlo methods. Our results demonstrate that the onset of absorbance and transmittance of these layers can be considerably tuned in the sub-micrometer range by controlling particle orientation in the layer. This high degree of tunability motivates experimental exploration into layers with oriented anisotropic $CuSbS_2$ nanoparticles at low volume fraction. Such films are promising candidates for solar cells, sensors, and related applications in the NIR regime.

Acknowledgments. This work was performed as part of the Academy of Finland project 314488 and QTF Centre of Excellence program (project 312298). We acknowledge computational resources provided by CSC – IT Center for Science (Finland) and by the Aalto Science-IT project (Aalto University School of Science).

Disclosures. There are no conflicts of interest for any of the authors in this work.

Supplemental document. See Supplement for discussion of the depolarization factor for spheroids, the magnitude of the total electric field at the corresponding scattering maxima and the absorption and scattering cross-sections at arbitrary angles of incidence.

REFERENCES

1. E. Peccerillo and K. Durose, "Copper–antimony and copper–bismuth chalcogenides—research opportunities and review for solar photovoltaics," MRS Energy Sustain. **5**, 1–59 (2018).
2. K. Takei, T. Maeda, and T. Wada, "Crystallographic and optical properties of $CuSbS_2$ and $CuSb(S_{1-x}Se_x)_2$ solid solution," Thin Solid Films **582**, 263–268 (2015).
3. F. W. de Souza Lucas, H. Peng, S. Johnston, P. C. Dippo, S. Lany, L. H. Mascaro, and A. Zakutayev, "Characterization of defects in copper antimony disulfide," J. Mater. Chem. A **5**, 21986–21993 (2017).
4. B. Yang, L. Wang, J. Han, Y. Zhou, H. Song, S. Chen, J. Zhong, L. Lv, D. Niu, and J. Tang, "$CuSbS_2$ as a promising earth-abundant photovoltaic absorber material: a combined theoretical and experimental study," Chem. Mater. **26**, 3135–3143 (2014).
5. J. Bincy, G. G. Silvena, and A. L. Rajesh, "Temperature dependent solvothermal synthesis of Cu-Sb-S nanoparticles with tunable structural and optical properties," Mater. Res. Bull. **95**, 267–276 (2017).
6. L. Wan, C. Ma, K. Hu, R. Zhou, X. Mao, S. Pan, L. H. Wong, and J. Xu, "Two-stage co-evaporated $CuSbS_2$ thin films for solar cells," J. Alloys Compd. **680**, 182–190 (2016).
7. C. Yan, Z. Su, E. Gu, T. Cao, J. Yang, J. Liu, F. Liu, Y. Lai, J. Li, and Y. Liu, "Solution-based synthesis of chalcostibite ($CuSbS_2$) nanobricks for solar energy conversion," RSC Adv. **2**, 10481–10484 (2012).
8. S. Moosakhani, A. A. S. Alvani, R. Mohammadpour, P.-M. Hannula, Y. Ge, and S.-P. Hannula, "Platelet $CuSbS_2$ particles with a suitable conduction band position for solar cell applications," Mater. Lett. **215**, 157–160 (2018).
9. J. T. Dufton, A. Walsh, P. M. Panchmatia, L. M. Peter, D. Colombara, and M. S. Islam, "Structural and electronic properties of $CuSbS_2$ and $CuBiS_2$: Potential absorber materials for thin-film solar cells," Phys. Chem. Chem. Phys. **14**, 7229–7233 (2012).
10. D. J. Temple, A. B. Kehoe, J. P. Allen, G. W. Watson, and D. O. Scanlon, "Geometry, electronic structure, and bonding in $CuMCh_2$ (M= Sb, Bi; Ch= S, Se): Alternative solar cell absorber materials?" J. Phys. Chem. C **116**, 7334–7340 (2012).
11. K. Ramasamy, H. Sims, W. H. Butler, and A. Gupta, "Mono-, few-, and multiple layers of copper antimony sulfide ($CuSbS_2$): A ternary layered sulfide," J. Am. Chem. Soc. **136**, 1587–1598 (2014).
12. A. Gassoumi, M. Musa Saad H.-E, S. Alfaify, T. Ben Nasr, and N. Bouarissa, "The investigation of crystal structure, elastic and optoelectronic properties of $CuSbS_2$ and $CuBiS_2$ compounds for photovoltaic applications," J. Alloys Compd. **725**, 181–189 (2017).
13. K. M. Conley, C. Cocchi, and T. Ala-Nissila, "Formation of near-IR excitons in low dimensional $CuSbS_2$," J. Phys. Chem. C **125**, 21087–21092 (2021).
14. W. Septina, S. Ikeda, Y. Iga, T. Harada, and M. Matsumura, "Thin film solar cell based on $CuSbS_2$ absorber fabricated from an electrochemically deposited metal stack," Thin Solid Films **550**, 700–704 (2014).
15. A. W. Welch, P. P. Zawadzki, S. Lany, C. A. Wolden, and A. Zakutayev, "Self-regulated growth and tunable properties of solar absorbers," Sol. Energy Mater Sol. Cells **132**, 499–506 (2015).
16. A. Rabhi, M. Kanzari, and B. Rezig, "Optical and structural properties of $CuSbS_2$ thin films grown by thermal evaporation method," Thin Solid Films **517**, 2477–2480 (2009).
17. R. Suriakarthick, V. N. Kumar, T. Shyju, and R. Gopalakrishnan, "Effect of substrate temperature on copper antimony sulphide thin films from thermal evaporation," J. Alloys Compd. **651**, 423–433 (2015).
18. C. Macías, S. Lugo, Á. Benítez, I. López, B. Kharissov, A. Vázquez, and Y. Peña, "Thin film solar cell based on $CuSbS_2$ absorber prepared by chemical bath deposition (CBD)," Mater. Res. Bull. **87**, 161–166 (2017).
19. J. Zhou, G.-Q. Bian, Q.-Y. Zhu, Y. Zhang, C.-Y. Li, and J. Dai, "Solvothermal crystal growth of $CuSbQ_2$(Q= S, Se) and the correlation between macroscopic morphology and microscopic structure," J. Solid State Chem. **182**, 259–264 (2009).
20. K. Ramasamy, R. K. Gupta, S. Palchoudhury, S. Ivanov, and A. Gupta, "Layer-structured copper antimony chalcogenides ($CuSbSe_xS_{2-x}$): Stable electrode materials for supercapacitors," J. Mater. Chem. **27**, 379–386 (2015).
21. Y. Zou and J. Jiang, "Colloidal synthesis of chalcostibite copper antimony sulfide nanocrystals," Mater. Lett. **123**, 66–69 (2014).
22. S. Moosakhani, A. A. S. Alvani, R. Mohammadpour, Y. Ge, and S.-P. Hannula, "Solution synthesis of $CuSbS_2$ nanocrystals: A new approach to control shape and size," J. Alloys Compd. **736**, 190–201 (2018).
23. A. Kabashin, P. Evans, S. Pastkovsky, W. Hendren, G. Wurtz, R. Atkinson, R. Pollard, V. Podolskiy, and A. Zayats, "Plasmonic nanorod metamaterials for biosensing," Nat. Mater. **8**, 867 (2009).
24. H. Matsui, W. Badalawa, A. Ikehata, and H. Tabata, "Oxide surface plasmon resonance for a new sensing platform in the near-infrared range," Adv. Opt. Mater. **1**, 397–403 (2013).
25. T. C. Preston and R. Signorell, "Preparation and optical properties of metallodielectric core- shell- corona particles," J. Phys. Chem. C **112**, 17844–17848 (2008).
26. A. Sousa-Castillo, Ó. Ameneiro-Prieto, M. Comesaña-Hermo, R. Yu, J. M. Vila-Fungueiriño, M. Pérez-Lorenzo, F. Rivadulla, F. J. G. de Abajo, and M. A. Correa-Duarte, "Hybrid plasmonic nanoresonators as efficient solar heat shields," Nano Energy **37**, 118–125 (2017).
27. G. Jönsson, D. Tordera, T. Pakizeh, M. Jaysankar, V. Miljkovic, L. Tong, M. P. Jonsson, and A. Dmitriev, "Solar transparent radiators by optical nanoantennas," Nano Lett. **17**, 6766–6772 (2017).
28. C. F. Bohren and D. R. Huffman, *A Potpourri of Particles* (John Wiley & Sons, New York, 1983), pp. 181–183.
29. F. Seyedheydari, K. Conley, and T. Ala-Nissila, "Near-IR plasmons in micro and nanoparticles with a semiconductor core," Photonics **7**, 10 (2020).
30. F. Seyedheydari, K. M. Conley, V. Thakore, M. Karttunen, A. Sihvola, and T. Ala-Nissila, "Electromagnetic response of nanoparticles with a metallic core and a semiconductor shell," J. Phys. Commun. **5**, 015002 (2021).
31. K. M. Conley, V. Thakore, F. Seyedheydari, M. Karttunen, and T. Ala-Nissila, "Directing near-infrared photon transport with core-shell particles," AIP Adv. **10**, 095128 (2020).
32. K. Conley, S. Moosakhani, V. Thakore, Y. Ge, J. Lehtonen, M. Karttunen, S.-P. Hannula, and T. Ala-Nissila, "Silica-silicon composites for near-infrared reflection: A comprehensive computational and experimental study," Ceram. Int. **47**, 16833–16840 (2021).
33. F. Seyedheydari, K. Conley, P. Ylä-Oijala, A. Sihvola, and T. Ala-Nissila,

"Electromagnetic response and optical properties of spherical $CuSbS_2$ nanoparticles," in *2021 Photonics Electromagnetics Research Symposium (PIERS),* (2021), pp. 2573–2578.
34. M. Kerker, *The scattering of light and other electromagnetic radiation: Physical chemistry: A series of monographs*, vol. 16 (Academic press, 2013).
35. D. Tzarouchis and A. Sihvola, "Light scattering by a dielectric sphere: Perspectives on the Mie resonances," Appl. Sci. **8**, 184 (2018).
36. N. Razmjooei, Y. H. Ko, F. A. Simlan, and R. Magnusson, "Resonant reflection by microsphere arrays with AR-quenched Mie scattering," Opt. Express **29**, 19183–19192 (2021).
37. E. B. Guidez and C. M. Aikens, "Quantum mechanical origin of the plasmon: From molecular systems to nanoparticles," Nanoscale **6**, 11512–11527 (2014).
38. P. D. Terekhov, K. V. Baryshnikova, Y. A. Artemyev, A. Karabchevsky, A. S. Shalin, and A. B. Evlyukhin, "Multipolar response of nonspherical silicon nanoparticles in the visible and near-infrared spectral ranges," Physical Review B **96**, 035443 (2017).
39. D. R. Dadadzhanov, T. A. Vartanyan, P. S. Parfenov, M. A. Baranov, and A. Karabchevsky, "Broadband plasmonic nanoparticles: fabrication, optical properties, and implications in liquid light chemiluminescence enhancement," arXiv preprint arXiv:1904.06462 (2019).
40. J. Volakis and K. Sertel, *Integral Equation Methods for Electromagnetics* (SciTech Publishing, Raleigh, NC., 2012).
41. P. Ylä-Oijala, J. Markkanen, S. Järvenpää, and S. Kiminki, "Surface and volume integral equation methods for time-harmonic solutions of Maxwell's equations," Progr. Electromagn. Research **149**, 15–44 (2014).
42. P. Ylä-Oijala and S. Järvenpää, New trends in frequency domain surface integral equations; in *New Trends in Computational Electromagnetics,* Edited by Ö. Ergül (SciTech Publishing, London, 2019).
43. J. Heyd, G. E. Scuseria, and M. Ernzerhof, "Hybrid functionals based on a screened coulomb potential," J. Chem. Phys. **118**, 8207–8215 (2003).
44. A. H. Barr, "Superquadrics and angle-preserving transformations," IEEE Comput. Graph. Appl. **1**, 11–23 (1981).
45. P. Ylä-Oijala, B. Kong, and S. Järvenpää, "Modeling of resonating closed impedance bodies with surface integral equation methods," IEEE Trans. Antennas Propag. **67**, 361–368 (2018).
46. J. Tang, V. Thakore, and T. Ala-Nissila, "Plasmonically enhanced reflectance of heat radiation from low-bandgap semiconductor microinclusions," Sci. Rep. **7**, 5696 (2017).
47. L. Wang, S. L. Jacques, and L. Zheng, "MCML-Monte Carlo modeling of light transport in multi-layered tissues," Comput Methods Programs Biomed. **47**, 131–146 (1995).
48. S. Merikallio, "Computer modeling of light scattering by atmospheric dust particles with spheroids and ellipsoids," Ph.D. thesis, Aalto University (2016).
49. A. Sihvola, *Electromagnetic Mixing Formulas and Applications* (The Institution of Electrical Engineers, London, 1999).
50. P. Ravindran, A. Delin, B. Johansson, O. Eriksson, and J. Wills, "Electronic structure, chemical bonding, and optical properties of ferroelectric and antiferroelectric $NaNO_2$," Phys. Rev. B **59**, 1776 (1999).
51. A. Reshak, S. A. Khan, and Z. Alahmed, "Investigation of electronic structure and optical properties of $MgAl_2O_4$: DFT approach," Opt. Mater. **37**, 322–326 (2014).